ACS APPLIED ENERGY MATERIALS

www.acsaem.org Article

Reversible Hydrogen Storage Performance of $2LiBH_4$-MgH_2 Enabled by Dual Metal Borides

Wei Chen, Yahui Sun, Tian Xu, Jikai Ye, Guanglin Xia,* Dalin Sun, and Xuebin Yu*

Cite This: https://doi.org/10.1021/acsaem.2c01142 Read Online

ACCESS | Metrics & More | Article Recommendations | Supporting Information

ABSTRACT: $2LiBH_4$-MgH_2 is a typical reactive hydride composite with a capacity of 11.5 wt % that has attracted intensive attention. Its practical application, however, is hindered by sluggish kinetics, poor reversibility, and different reaction pathways under various temperatures and hydrogen back pressures. Herein, bimetallic (NiCo) sheet-like nanoporous carbon (NiCo@NC) is designed to improve the hydrogen storage performance of $2LiBH_4$-MgH_2 composite. During the initial H_2 desorption process of $2LiBH_4$-MgH_2 under 4 atm H_2 pressure, NiCo NPs in NiCo@NC would be *in situ* transformed into $MgNi_3B_2$, acting as the heterogeneous nucleation sites for MgB_2, and CoB, serving as the effective catalyst for H_2 desorption of $2LiBH_4$-MgH_2 composite. Due to the synergistic effect of *in situ* formed CoB and $MgNi_3B_2$, the incubation period for $2LiBH_4$-MgH_2 is reduced to 1.5 h in the initial H_2 desorption process and almost vanished in the following H_2 desorption and adsorption cycles, while the incubation time for bulk $2LiBH_4$-MgH_2 composite reaches 16 h. More importantly, induced by the catalysis of NiCo@NC, $2LiBH_4$-MgH_2 exhibits improved cycling stability with a reversible capacity of 8.4 wt % after 10 cycles of hydrogen storage process, corresponding to 95.5% of H_2 desorption capacity of the second cycle. This work provides a potential strategy for the design of dual-functional catalysts to improve reversible hydrogen storage performance of reactive hydride composites.

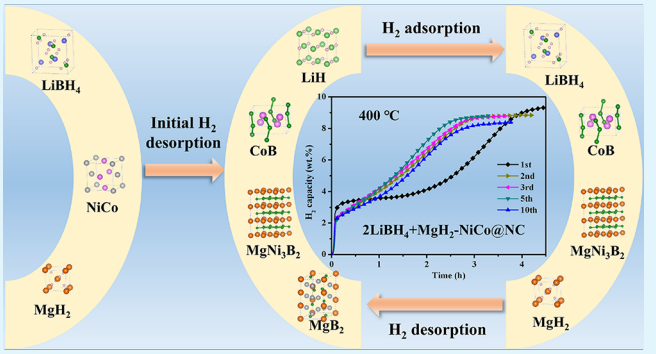

KEYWORDS: *hydrogen storage, MgH_2, $LiBH_4$, reactive hydride composite, metal borides*

1. INTRODUCTION

Hydrogen storage has been widely regarded as one of the most important challenges in the implementation of so-called "hydrogen economy".[1−3] It depends critically on the advanced hydrogen storage materials, which could realize the effective and efficient storage of H_2 on-board with high gravimetric and volumetric densities.[3−6] In recent years, complex hydrides attract considerable attention as potential hydrogen storage materials due to their high gravimetric and volumetric hydrogen densities.[7−10] Among them, the gravimetric hydrogen density of lithium borohydride ($LiBH_4$) reaches 18.5 wt %.[11] The practical application of $LiBH_4$, however, is strictly hindered by its high thermodynamic stability and sluggish kinetics.[12−14] More importantly, the formation of inactive element boron and intermediate compound $Li_2B_{12}H_{12}$ after dehydrogenation results in the extremely poor reversibility of $LiBH_4$ even under harsh conditions.[15,16] As a result, the reactive hydride composite composed of $LiBH_4$ and MgH_2 has been developed, in which $LiBH_4$ could be thermodynamically destabilized by MgH_2 *via* the formation of MgB_2 with favorable adsorption capability of H_2 as the dehydrogenation product.[16,17] Hence, in comparison with pure $LiBH_4$, the H_2 desorption enthalpy could be reduced by ∼21 kJ mol^{-1} H_2 based on the two-step reaction pathways (eq 1), which thermodynamically improves the reversibility of hydrogen storage reaction under moderate conditions.[18−20]

$$2LiBH_4 + MgH_2 \rightarrow 2LiBH_4 + Mg + H_2 \rightarrow 2LiH + MgB_2 + 3H_2 \quad (1)$$

Unfortunately, owing to the nucleation restriction of MgB_2 during the second step, an ultralong incubation period (*e.g.*, up to 25 h at 400 °C under 5 atm of hydrogen) is required in general, thereby resulting in an extraordinarily sluggish kinetics.[21] It poses a major bottleneck for the development of $2LiBH_4$-MgH_2 composite as practical hydrogen storage materials. On the other hand, the dehydrogenation reaction of $2LiBH_4$-MgH_2 composite is highly dependent on the temperature and hydrogen back pressure. It has been found that the

Received: April 18, 2022
Accepted: August 19, 2022

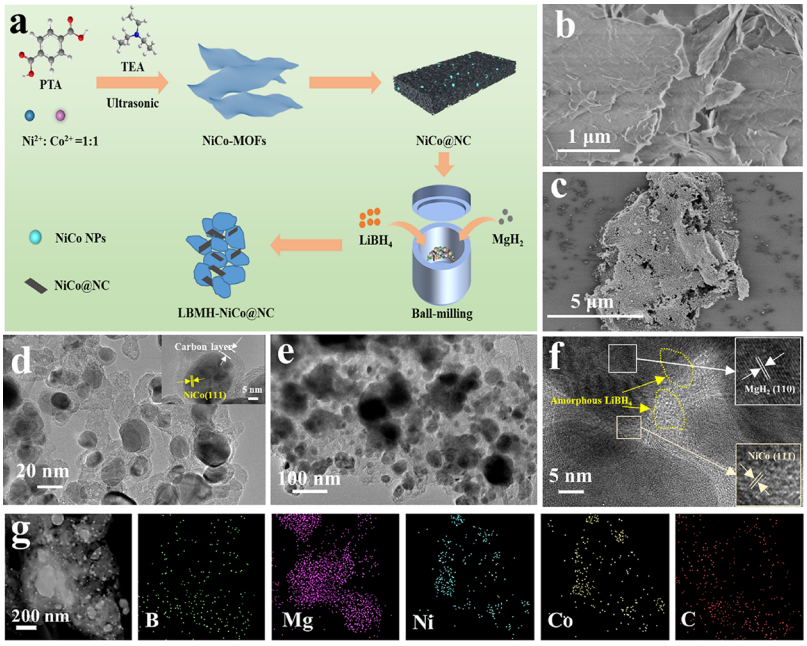

Figure 1. (a) Schematic diagram of the fabrication process of LBMH-NiCo@NC. SEM images of (b) NiCo-MOFs and (c) NiCo@NC. (d) TEM and HRTEM (inset) images of NiCo@NC. (e) TEM and (f) HRTEM images of LBMH-NiCo@NC. (g) STEM and the corresponding EDS elemental mapping images of LBMH-NiCo@NC.

modification of suitable hydrogen back-pressure could avoid the individual decomposition of $LiBH_4$ and simultaneously facilitate the mutual reaction between $LiBH_4$ and MgH_2, which promotes the hydrogen desorption from $2LiBH_4$-MgH_2 composite through eq 1.

One of the most effective strategies to improve the hydrogen storage performance of $2LiBH_4$-MgH_2 composite is the introduction of metal-based catalysts, including metal halides, metal oxides, and metal sulfides.[22−28] Induced by the high reactivity of MgH_2 and $LiBH_4$, these metal-based catalysts would be transformed to stable metallic borides in general, which are able to reduce the operating temperature and simultaneously promote the kinetics of hydrogen desorption and adsorption process of $2LiBH_4$-MgH_2 composite.[28−30] For instance, it has been demonstrated that the formation of CoB from the interaction between Co and $LiBH_4$ plays a catalytic role in improving the H_2 desorption and adsorption of $2LiBH_4$-MgH_2 and promoting the formation of MgB_2, which results in the reduction of incubation period down to only 4 h.[29] Interestingly, during the dehydrogenation process of Ni-catalyzed $2LiBH_4$-MgH_2 composite, the formation of $MgNi_3B_2$ is identified as the heterogeneous nucleation sites for the formation of MgB_2, which could also facilitate the dehydrogenation kinetics of $2LiBH_4$-MgH_2 composite.[29] Despite these intense research efforts, the high operating temperature for the reversible hydrogen storage of $2LiBH_4$-MgH_2 composite with a long incubation period still hinders its practical application.[31−33] Therefore, the development of advanced catalysts to improve H_2 desorption and adsorption performance of $2LiBH_4$-MgH_2 composite is highly desirable but remains a great challenge.

Inspired by the role of CoB in catalytically improving the hydrogen storage performance of $2LiBH_4$-MgH_2 composite and the role of $MgNi_3B_2$ in serving as the heterogenous nucleation sites for the formation of MgB_2, a bimetallic (NiCo) sheet-like nanoporous carbon (denoted as NiCo@NC) is prepared to improve the hydrogen storage performance of $2LiBH_4$-MgH_2 composite, which could result in simultaneous formation of CoB and $MgNi_3B_2$ during the initial H_2 desorption process. As a result, under the catalytic effect of NiCo@NC, the $2LiBH_4$-MgH_2 composite could release 9.4 wt % of H_2 within 4.5 h in the initial H_2 desorption process with an incubation time of only 1.5 h, and interestingly, the incubation period is almost vanished during the following H_2 desorption and adsorption cycles. By comparison, an ultralong incubation time of 16 h, 10.7 times of $2LiBH_4$-MgH_2 composite under the catalysis of NiCo@NC, is observed for bulk $2LiBH_4$-MgH_2 composite. More importantly, a reversible H_2 storage capacity of 8.4 wt % could be maintained for $2LiBH_4$-MgH_2 catalyzed by NiCo@NC after 10 cycles of H_2 desorption and adsorption process, corresponding to 95.5% of H_2 desorption capacity of the second cycle.

2. RESULTS AND DISCUSSION

As schematically illustrated in Figure 1a, the ultrathin metal−organic framework nanosheets (denoted as NiCo-MOFs), which could be directly revealed by scanning electron microscopy (SEM) images (Figure 1b), are first synthesized from a mixed solution of Ni^{2+}, Co^{2+}, terephthalic acid (PTA), and triethylamine (TEA) by a previously reported ultrasonication method.[34,35] X-ray diffraction (XRD) patterns confirm the formation of NiCo-MOFs with a space group of *C*2/*m* (Figure S1).[36] After carbonization under a dynamic Ar atmosphere, the typical diffraction peaks of NiCo-MOFs completely disappear and new peaks that could be indexed to NiCo alloys could be observed in the XRD patterns (Figure S1) of thus-obtained NiCo@NC, which inherits the sheet-like structure of NiCo-MOFs (Figure 1c). Transmission electron microcopy (TEM) results (Figure 1d) reveal the uniform distribution of NiCo NPs that have particle sizes distributed between 15 and 30 nm in NiCo@NC. The high-resolution TEM (HRTEM) image (inset of Figure 1d) illustrates a clear

https://doi.org/10.1021/acsaem.2c01142
ACS Appl. Energy Mater. XXXX, XXX, XXX−XXX

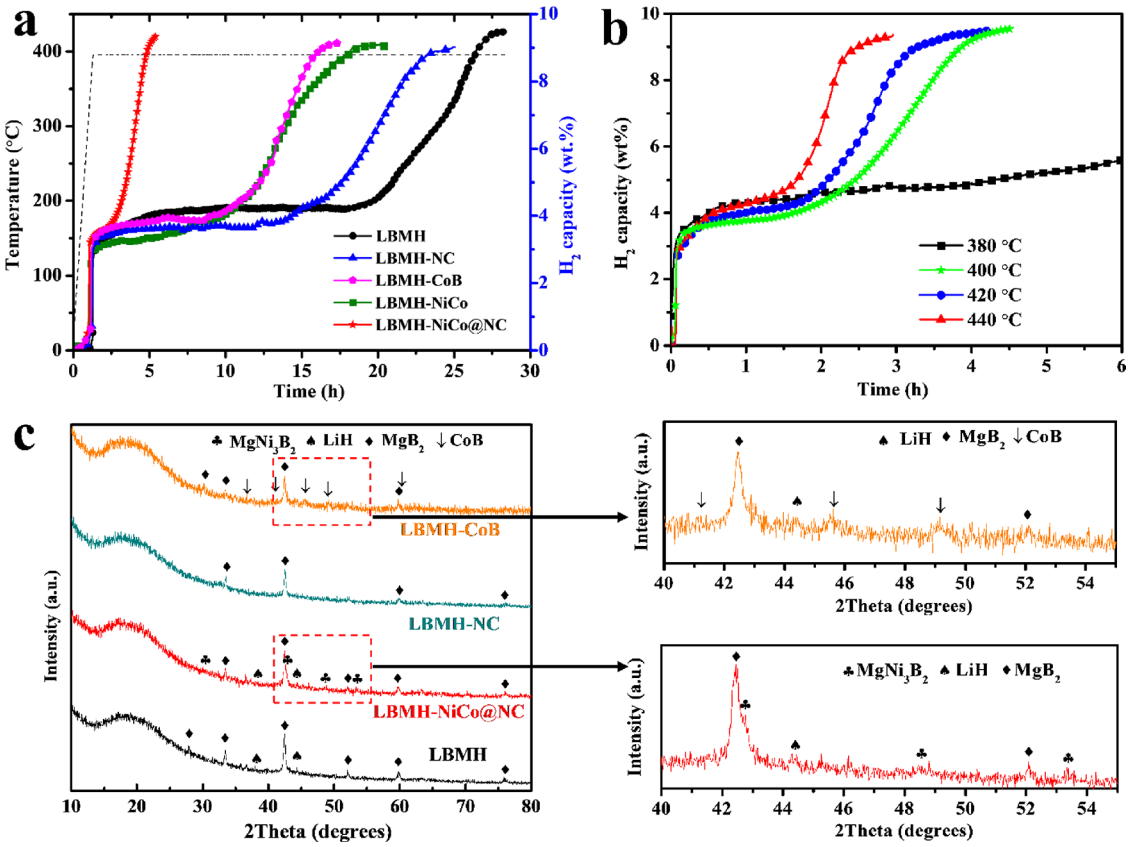

Figure 2. (a) H_2 desorption curves of LBMH-NiCo@NC under a hydrogen pressure of 4 atm, with LBMH, LBMH-NiCo, LBMH-CoB, and LBMH-NC included for comparison. (b) Isothermal H_2 desorption kinetics of LBMH-NiCo@NC at various temperatures under a hydrogen pressure of 4 atm. (c) XRD patterns of LBMH, LBMH-NiCo@NC, LBMH-NC, and LBMH-CoB after the initial H_2 desorption process at 400 °C under a hydrogen pressure of 4 atm.

lattice spacing of 0.204 nm of the (111) plane of NiCo alloys that are homogeneously coated with ultrathin carbon layers, which demonstrates the synthesis of NiCo alloys after carbonization. The coating of ultrathin carbon layers could preserve the agglomeration NiCo NPs during the ball-milling process and inhibit the particle growth of NiCo NPs upon subsequent thermal heating during a repeated H_2 adsorption and desorption process. The fitting peaks at approximately 852.5 and 869.9 eV in high-resolution Ni 2p X-ray photoelectron spectroscopy (XPS) spectrum and two fitting peaks at approximately 778.3 and 793.4 eV in high-resolution Co 2p XPS spectrum could be indexed to NiCo alloys (Figure S2).[37]

To evaluate the effect of NiCo@NC in improving the hydrogen storage performance of $2LiBH_4$-MgH_2 composite, the as-prepared sheet-like NiCo@NC with a mass ratio of 10% is mixed with $2LiBH_4$-MgH_2 composite *via* mechanical milling (denoted as LBMH-NiCo@NC). SEM (Figure S3) and TEM measurements (Figure 1e) indicate the relatively uniform distribution of sheet-like NiCo@NC into $2LiBH_4$-MgH_2 composite. After the milling process, the characteristic peaks of MgH_2 and NiCo alloy could be clearly observed in the XRD results of LBMH-NiCo@NC (Figure S4), whereas no peaks of $LiBH_4$ could be detected, indicating the amorphous nature of $LiBH_4$. Fortunately, the presence of $LiBH_4$ with its typical absorption peaks could be verified by the detection of Fourier transform infrared spectroscopy (FTIR) (Figure S5). The presence of typical lattice planes of MgH_2 and NiCo alloys in the HRTEM image (Figure 1f) coincides well with XRD results (Figure S4). According to the EDS elemental mapping results (Figure 1g), the signals of Ni, Co, and C of NiCo@NC overlap well with those of Mg of MgH_2 and B of $LiBH_4$, which provides direct evidence to the uniform distribution between NiCo@NC and $2LiBH_4$-MgH_2 composite.

The H_2 desorption performance of LBMH-NiCo@NC is subsequently investigated under a hydrogen pressure of 4 atm with a heating rate of 5 °C min^{-1} (Figure 2a). Owing to the sluggish H_2 desorption kinetics and longstanding nucleation period of MgB_2, the complete dehydrogenation of the ball-milled $2LiBH_4$-MgH_2 composite (denoted as LBMH) is realized within a period of over 28 h, exhibiting an incubation time of as long as 16 h. It is interesting to note that the nucleation period for $2LiBH_4$-MgH_2 could be reduced to less than 7 h after the addition of NiCo NPs (denoted as LBMH-NiCo), and this phenomenon could also be observed for $2LiBH_4$-MgH_2 composite with the addition of NiCo@NC after the etching of NiCo NPs (denoted as LBMH-NC). This result indicates the catalytic role of both NiCo NPs and carbon nanosheets in enhancing the H_2 desorption performance of $2LiBH_4$-MgH_2 composite. As a result, induced by the introduction of NiCo@NC, the nucleation period for $2LiBH_4$-MgH_2 could be impressively reduced to approximately 1.5 h, and only 5 h is required for the complete dehydrogenation of LBMH-NiCo@NC, indicating the synergistic role of NiCo NPs and carbon nanosheets of NiCo@NC with uniform distribution in facilitating the H_2 desorption process of $2LiBH_4$-MgH_2 composite. To further verify the catalytic role of NiCo@NC, the H_2 desorption kinetics of LBMH-NiCo@NC at various temperatures is evaluated in detail. As shown in

https://doi.org/10.1021/acsaem.2c01142
ACS Appl. Energy Mater. XXXX, XXX, XXX−XXX

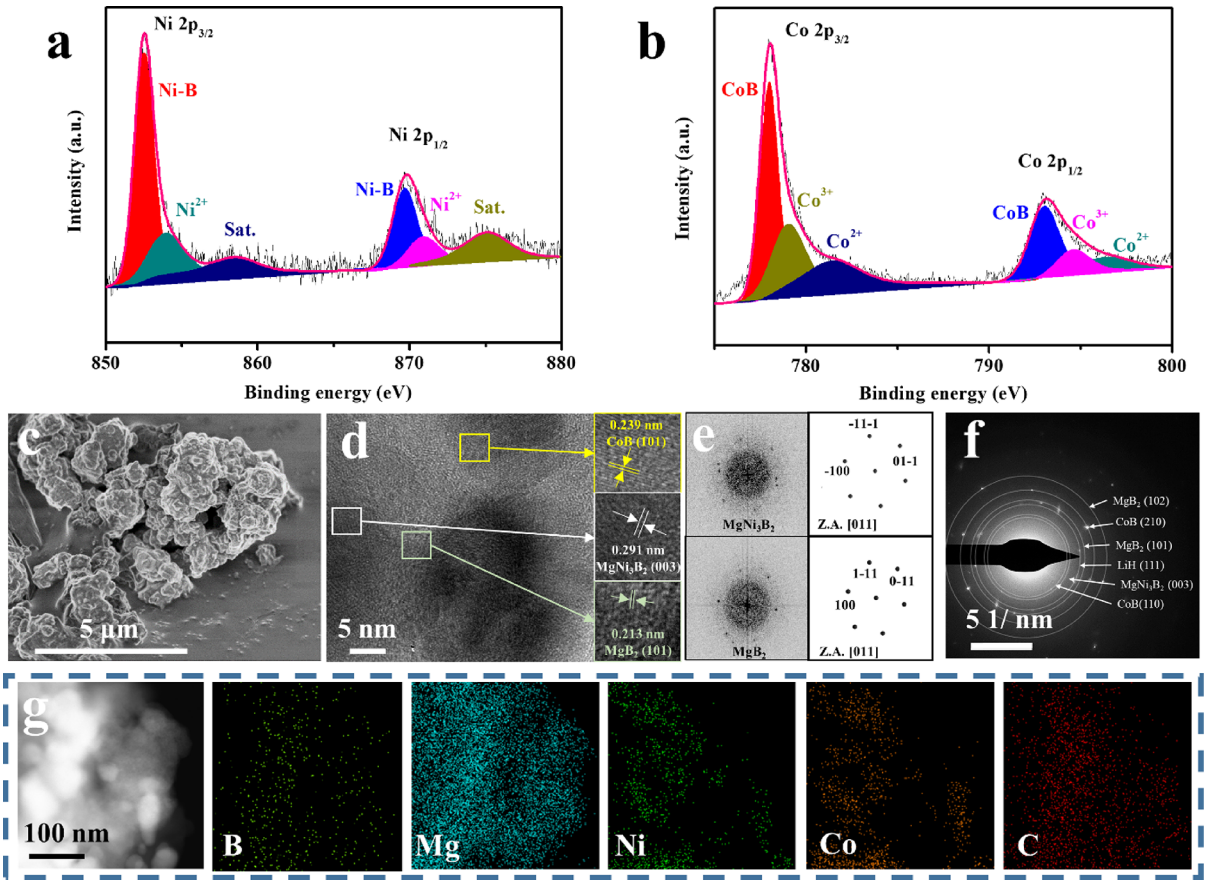

Figure 3. High-resolution (a) Ni 2p and (b) Co 2p XPS spectra, (c) SEM, (d) HRTEM, and relative (e) FFT and simulated FFT patterns and (f) SAED pattern of LBMH-NiCo@NC after the initial H_2 desorption process. (g) STEM and the relative elemental mapping images of LBMH-NiCo@NC after the initial H_2 desorption process.

Figure 2b, 5.5 wt % of H_2 could be released within 6 h even at a temperature as low as 380 °C and only 3.5 h was required for the complete H_2 desorption of LBMH-NiCo@NC upon increasing the operating temperature to 420 °C. By comparsion, an ultralong time of 11 h, 3.1 times that of LBMH-NiCo@NC, is required for the full decomposition of LBMH under identical conditions at 420 °C (Figure S6). Specifically, upon decreasing the operating temperature down to 400 °C, 9.4 wt % hydrogen could be released from LBMH-NiCo@NC within 4.5 h, which further demonstrates the superior catalytic role of NiCo@NC in improving H_2 desorption kinetics of $2LiBH_4$-MgH_2 composite.

To reveal the mechanism behind this enhancement, the dehydrogenation products of LBMH-NiCo@NC are investigated. As shown in Figure 2c, the XRD patterns exhibit the diffraction peaks of LiH and MgB_2 with the complete disappearance of the typical peaks of B−H vibrations in FTIR results after the H_2 desorption process at 400 °C (Figure S7), indicating the complete dehydrogenation of the $2LiBH_4$-MgH_2 composite. It is interesting to note that, in addition to the presence of LiH and MgB_2, new diffraction peaks indexed to $MgNi_3B_2$ could be observed in the magnified XRD patterns of LBMH-NiCo@NC after complete dehydrogenation, which could be further supported by high-resolution Ni 1p XPS spectrum (Figure 3a),[38] verifying the formation of $MgNi_3B_2$ after the initial H_2 desorption process. The as-formed $MgNi_3B_2$ has been identified as the heterogeneous nucleation sites for MgB_2, which hence is capable of facilitating H_2 desorption kinetics of $2LiBH_4$-MgH_2 composite.[28−30,38] In addition, the binding energies at 778 and 793.6 eV in Co 2p XPS spectrum (Figure 3b) and 187.9 eV in B 1s XPS spectrum (Figure S8) provide further evidence to the formation of CoB upon the H_2 desorption process.[39] Hence, in addition to the H_2 desorption pathway, as shown in eq 1, the reaction between $2LiBH_4$-MgH_2 composite and NiCo@NC during the initial dehydrogenation process of $2LiBH_4$-MgH_2 composite upon heating to 400 °C under a hydrogen pressure of 4 atm could be involved according to eq 2, as shown below.

$$12LiBH_4 + 3MgH_2 + 6NiCo \rightarrow 12LiH + MgB_2 + 2MgNi_3B_2 + 6CoB + 21H_2 \quad (2)$$

Interestingly, after the addition of CoB NPs (denoted as LBMH-CoB), the nucleation period for H_2 desorption from $2LiBH_4$-MgH_2 composite could be significantly decreased to 7 h (Figure 2a), which directly confirms the catalytic role of CoB in improving the H_2 desorption performance of $2LiBH_4$-MgH_2 composite. Moreover, upon elevating the temperature to 420 and 440 °C, the XRD results (Figure S9) of the dehydrogenated products of LBMH-NiCo@NC, which reveal the formation of MgB_2 accompanied with the detection of CoB and $MgNi_3B_2$, are comparable to those upon heating at 400 °C, indicating that the dehydrogenation pathway of LBMH-NiCo@NC remains unchanged upon heating from 400 to 440 °C. In addition, the characteristic peaks of the B−H bonds of LBMH-NiCo@NC disappear completely in the FTIR

https://doi.org/10.1021/acsaem.2c01142
ACS Appl. Energy Mater. XXXX, XXX, XXX−XXX

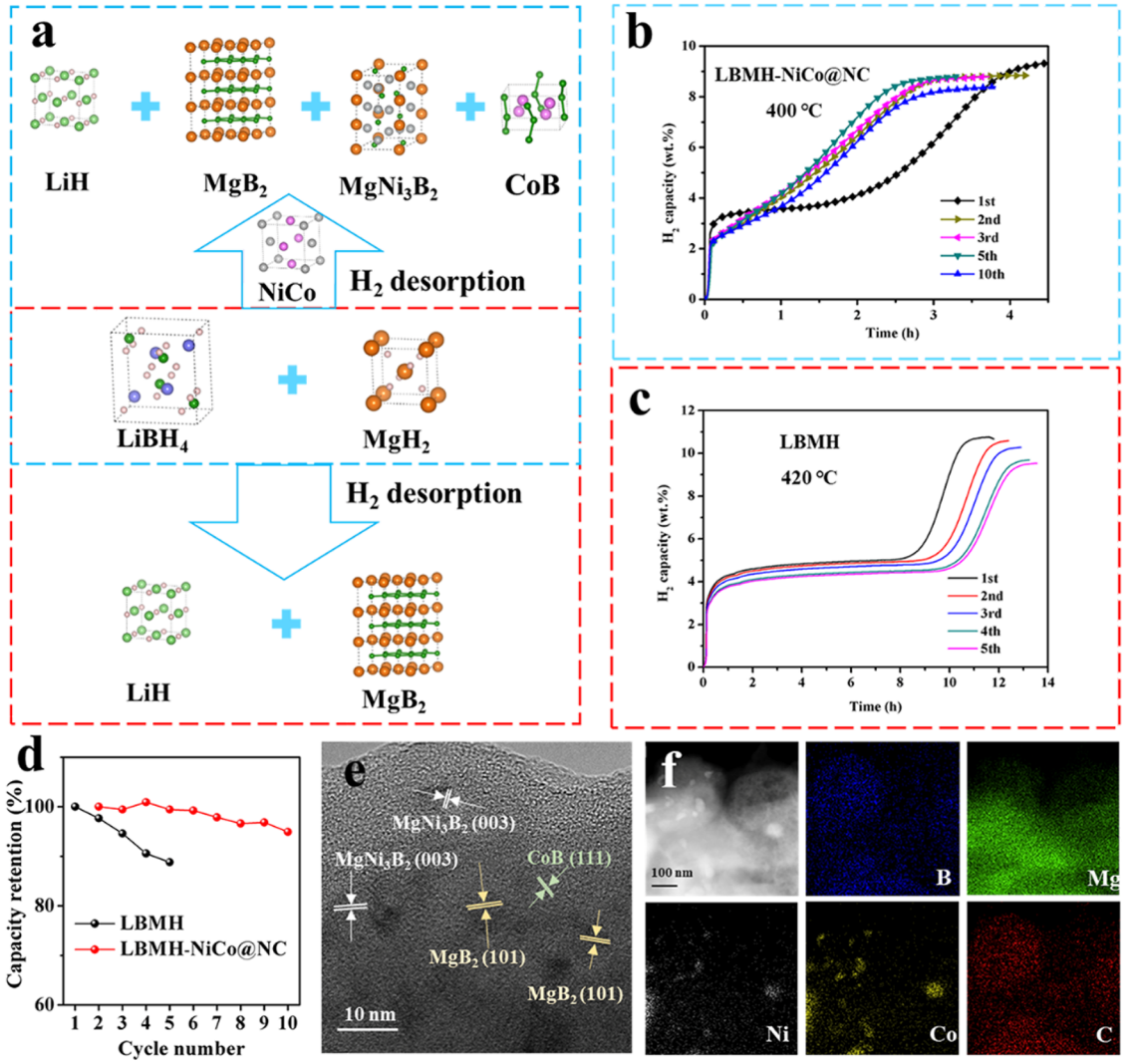

Figure 4. (a) Schematic illustration of H_2 storage reaction of $2LiBH_4$-MgH_2 composite under the catalysis of NiCo@NC. Cycling H_2 desorption performance of (b) LBMH-NiCo@NC at 400 °C and (c) LBMH at 420 °C under a hydrogen pressure of 4 atm. Hydrogen adsorption is performed at 350 °C under a hydrogen pressure of 60 atm for 10 h. (d) Capacity retention of LBMH-NiCo@NC corresponding to the H_2 desorption capacity of the second cycle, with $2LiBH_4$-MgH_2 composite included for comparison. (e) HRTEM image and (f) the corresponding EDS elemental mapping images of LBMH-NiCo@NC after 10 cycles of H_2 desorption process.

spectra (Figure S7) after heating from 400 to 440 °C, validating the complete dehydrogenation of LBMH-NiCo@NC, which corresponds well with their complete dehydrogenation performance with a H_2 desorption capacity that is comparable to their theoretical capacity (Figure 2b).

After the initial H_2 desorption process upon thermal heating, partial aggregation of LBMH-NiCo@NC could be observed in the SEM (Figure 3c) and TEM (Figure S10) images. The interplanar spacings of the as-formed nanoparticles observed in the HRTEM image (Figure 3d) are calculated to be 0.213, 0.239, and 0.291 nm, which could be indexed to the (101) plane of MgB_2, (101) plane of CoB, and (003) plane of $MgNi_3B_2$, respectively, which validates the uniform distribution of CoB and $MgNi_3B_2$ near the surface of MgB_2 with intimate contact. Figure 3e presents the fast-Fourier transform (FFT) diffraction patterns of the selected regions and the corresponding simulated FFT patterns. The FFT patterns of the thus-formed hexagonal $MgNi_3B_2$ and MgB_2 agree well with their respective simulated patterns, which provide additional evidence to the formation of $MgNi_3B_2$ and MgB_2. In addition, the selected area electron diffraction (SAED) of the dehydrogenated LBMH-NiCo@NC (Figure 3f) also illustrates the existence of LiH, MgB_2, $MgNi_3B_2$, and CoB, which is in good agreement with XRD (Figure 2c) and XPS (Figure 3a,b) results. In the relative EDS elemental mapping images (Figure 3f), the elements Mg, B, Ni, Co, and C are still homogeneously distributed, indicating the uniform distribution of thus-formed CoB and $MgNi_3B_2$ in the dehydrogenation products (*i.e.*, MgB_2). Since the nucleation of MgB_2 is the reaction rate-limiting step in the H_2 desorption process of $2LiBH_4$-MgH_2 composite, it has been widely regarded as an effective strategy to improve the H_2 desorption kinetics of $2LiBH_4$-MgH_2 composite by shortening the nucleation period of MgB_2.[30] In terms of $2LiBH_4$-MgH_2 composite under the catalysis of NiCo@NC, the *in situ* formed $MgNi_3B_2$ exhibits a hexagonal structure with a space group of $P6_222$ that is identical to the structure of MgB_2 (hexagonal, $P6/mmm$).[29,40] As a result, the formation and growth of MgB_2 could be facilitated around the surface of $MgNi_3B_2$ due to their comparable crystal structure as evidenced by the HRTEM result (Figure 3e), which hence

https://doi.org/10.1021/acsaem.2c01142
ACS Appl. Energy Mater. XXXX, XXX, XXX−XXX

would promote the H_2 desorption kinetics of $2LiBH_4$-MgH_2 composite. In addition, the simultaneously formed CoB plays a catalytic role in further enhancing the H_2 desorption kinetics of $2LiBH_4$-MgH_2 composite as evidenced by TPD results (Figure 2a).[28,29] Therefore, based on the synergistic effect of *in situ* formed dual metal borides, *i.e.*, $MgNi_3B_2$ and CoB, the H_2 desorption kinetics of $2LiBH_4$-MgH_2 composite is significantly improved.

Since the synergistic role of $MgNi_3B_2$ and CoB that are simultaneously formed during the initial H_2 desorption process of LBMH-NiCo@NC simultaneously contributes to enhancing the H_2 desorption performance of $2LiBH_4$-MgH_2 composite, the reversibility of LBMH-NiCo@NC is subsequently investigated to evaluate its cycling performance. As schematically illustrated in Figure 4a, owing to the addition of NiCo@NC, 9.4 wt % of H_2 could be released from LBMH-NiCo@NC at 400 °C within 4.5 h (Figure 4b), while the capacity is reduced to 8.9 wt % in the second cycle of H_2 desorption, which could be attributed to the consumption of $LiBH_4$ and MgH_2 due to the formation of CoB and $MgNi_3B_2$ from the reaction between $2LiBH_4$-MgH_2 and NiCo@NC. After rehydrogenation, the regeneration of MgH_2 could be clearly observed in the XRD results (Figure S11), accompanied with the detection of $MgNi_3B_2$ and CoB. Although no characteristic XRD peaks of $LiBH_4$ could be detected, the formation of $LiBH_4$ could be well supported by FTIR results (Figure S12), which reveal the typical peaks of the B−H bonds of $LiBH_4$, which provides additional evidence to the regeneration of $LiBH_4$ and MgH_2 with the existence of $MgNi_3B_2$ and CoB after rehydrogenation at 350 °C under 60 atm H_2 pressure. Interestingly, there is almost no nucleation period for LBMH-NiCo@NC from the second cycle of H_2 desorption due to the presence of thus-formed CoB and $MgNi_3B_2$ during the initial H_2 desorption process, which provides direct evidence to the synergistic role of $MgNi_3B_2$ and CoB in enhancing the H_2 desorption performance of $2LiBH_4$-MgH_2 composite. More importantly, the H_2 desorption capacity could be well preserved to be 8.4 wt % after 10 cycles of hydrogenation and dehydrogenation process, corresponding to 95.5% of H_2 desorption capacity of the second cycle (Figure 4d), indicating the excellent stability of $MgNi_3B_2$ and CoB upon the cycling hydrogen storage process. By contrast, an ultralong period of 12 h is required for the complete H_2 desorption of $2LiBH_4$-MgH_2 composite even at a temperature as high as 420 °C (Figure 4c) and a slight increase in the nucleation time would be observed in the subsequent H_2 desorption process due to the increase in particle sizes during cycling. In addition, the H_2 desorption capacity is also reduced to 9.5 wt % after only five cycles of H_2 storage process, which could be attributed to the particle aggregation upon heating at high temperatures and incomplete hydrogenation of the dehydrogenated products, corresponding to 88.8% of the initial capacity (Figure 4d).[17,41] By prolonging the hydrogenation time to 20 h, only a slight capacity decay of LBMH could be observed (Figure S6), which confirms the sluggish hydrogenation kinetics of LBMH and catalytic effect of *in situ* formed $MgNi_3B_2$ and CoB in enhancing the hydrogen adsorption performance of $2LiBH_4$-MgH_2 composite. Compared with the previously reported $2LiBH_4$-MgH_2 composite catalyzed by Ni-based catalysts, the capacity retention and the reversible capacity of LBMH-NiCo@NC are among the best Ni/Co-based catalyst-doped $2LiBH_4$-MgH_2 composite.

After 10 cycles of H_2 desorption process, HRTEM (Figure 4e) of LBMH-NiCo@NC illustrates the interplanar spacings of 0.213, 0.221, and 0.292 nm, corresponding to the (101) plane of MgB_2, (111) plane of CoB, and (003) plane of $MgNi_3B_2$, respectively, which directly confirms the excellent stability and uniform distribution of *in situ* formed CoB and $MgNi_3B_2$ around MgB_2 during the cycling H_2 storage process. Moreover, the elemental mapping of Ni, Co, and C of NiCo@NC matches well with that of B and Mg from $2LiBH_4$-MgH_2 composite (Figure 4f), which provides additional evidence to the homogeneous distribution of *in situ* formed CoB and $MgNi_3B_2$ during the cycling H_2 storage process. As a result, the H_2 desorption kinetics and H_2 storage capacity of $2LiBH_4$-MgH_2 composite under the catalysis of NiCo@NC could be well-preserved (Figure 4b).

3. CONCLUSIONS

In this work, a novel bimetallic (NiCo) sheet-like nanoporous carbon derived from ultrathin NiCo-MOFs nanosheets is fabricated to improve the reversible H_2 desorption and adsorption of $2LiBH_4$-MgH_2 composite. The initial H_2 desorption of $2LiBH_4$-MgH_2 composite with the catalysis of NiCo@NC under 4 atm H_2 pressure results in the *in situ* formation of both $MgNi_3B_2$, acting as the nucleation sites for the formation of MgB_2, and CoB, serving as the catalysts to promote the H_2 desorption kinetics of $2LiBH_4$-MgH_2 composite, which possess the same reaction pathway at temperatures lower than 440 °C. As a result, the incubation time for H_2 desorption of $2LiBH_4$-MgH_2 composite could be significantly reduced to only 1.5 h in the initial dehydrogenation process at 400 °C and it almost vanished in the following H_2 desorption and adsorption cycles owing to the excellent stability of *in situ* formed CoB and $MgNi_3B_2$. In strong contrast, the incubation time for H_2 desorption of bulk $2LiBH_4$-MgH_2 composite reaches 16 h at 400 °C, 10.7 times of that of $2LiBH_4$-MgH_2 composite under the catalysis of NiCo@NC. More importantly, a reversible H_2 desorption capacity of 8.4 wt % could be achieved for $2LiBH_4$-MgH_2 composite under the catalysis of NiCo@NC after 10 cycles, corresponding to 95.5% of H_2 desorption capacity of the second cycle. The synergistic role of dual metal borides that could serve as effective catalysts and nucleation sites developed in this work might open up new perspectives in improving the reversible hydrogen storage performance of reactive hydride composites.

■ ASSOCIATED CONTENT

Supporting Information

The Supporting Information is available free of charge at https://pubs.acs.org/doi/10.1021/acsaem.2c01142.

Experimental details and additional structural and hydrogen storage performance data (PDF)

■ AUTHOR INFORMATION

Corresponding Authors

Guanglin Xia − *Department of Materials Science, Fudan University, Shanghai 200433, China;* orcid.org/0000-0002-3493-4309; Email: xiaguanglin@fudan.edu.cn

Xuebin Yu − *Department of Materials Science, Fudan University, Shanghai 200433, China;* orcid.org/0000-0002-4035-0991; Email: yuxuebin@fudan.edu.cn

https://doi.org/10.1021/acsaem.2c01142
ACS Appl. Energy Mater. XXXX, XXX, XXX−XXX

Authors

Wei Chen − *Department of Materials Science, Fudan University, Shanghai 200433, China*

Yahui Sun − *Department of Materials Science, Fudan University, Shanghai 200433, China*

Tian Xu − *Department of Materials Science, Fudan University, Shanghai 200433, China*

Jikai Ye − *Department of Materials Science, Fudan University, Shanghai 200433, China*

Dalin Sun − *Department of Materials Science, Fudan University, Shanghai 200433, China*

Complete contact information is available at: https://pubs.acs.org/10.1021/acsaem.2c01142

Author Contributions

W.C. contributed in the investigation, methodology, characterization, and writing-original draft preparation. Y.S. contributed in the investigation and methodology. T.X. drew the figures. J.Y. contributed in the characterization. G.X. contributed in the methodology, writing-reviewing and editing. D.S. participated in writing-reviewing. X.Y. supervised the study and participated in writing-reviewing.

Notes

The authors declare no competing financial interest.

■ ACKNOWLEDGMENTS

This work was partially supported by the National Key R&D Program of China (no. 2020YFA0406204), the National Natural Science Foundation of China (51971065, 51901045, and U2130208), the Science and Technology Commission of Shanghai Municipality (no. 21ZR1407500), and the Innovation Program of Shanghai Municipal Education Commission (2019-01-07-00-07-E00028).

■ REFERENCES

(1) Schneemann, A.; White, J. L.; Kang, S.; Jeong, S.; Wan, L. F.; Cho, E. S.; Heo, T. W.; Prendergast, D.; Urban, J. J.; Wood, B. C.; Allendorf, M. D.; Stavila, V. Nanostructured metal hydrides for hydrogen storage. *Chem. Rev.* **2018**, *118*, 10775−10839.

(2) Chen, W.; Ju, S.; Sun, Y.; Zhang, T.; Wang, J.; Ye, J.; Xia, G.; Yu, X. Thermodynamically favored stable hydrogen storage reversibility of $NaBH_4$ inside of bimetallic nanoporous carbon nanosheets. *J. Mater. Chem. A* **2022**, *10*, 7122−7129.

(3) Wang, Y.; Chen, X.; Zhang, H.; Xia, G.; Sun, D.; Yu, X. Heterostructures built in metal hydrides for advanced hydrogen storage reversibility. *Adv. Mater.* **2020**, *32*, 2002647.

(4) Yu, X.; Tang, Z.; Sun, D.; Ouyang, L.; Zhu, M. Recent advances and remaining challenges of nanostructured materials for hydrogen storage applications. *Prog. Mater. Sci.* **2017**, *88*, 1−48.

(5) Zhu, Y.; Ouyang, L.; Zhong, H.; Liu, J.; Wang, H.; Shao, H.; Huang, Z.; Zhu, M. Closing the loop for hydrogen storage: facile regeneration of $NaBH_4$ from its hydrolytic product. *Angew. Chem., Int. Ed.* **2020**, *59*, 8623−8629.

(6) Xia, G.; Tan, Y.; Chen, X.; Sun, D.; Guo, Z.; Liu, H.; Ouyang, L.; Zhu, M.; Yu, X. Monodisperse magnesium hydride nanoparticles uniformly self-assembled on graphene. *Adv. Mater.* **2015**, *27*, 5981−5988.

(7) He, T.; Cao, H.; Chen, P. Complex hydrides for energy storage, conversion, and utilization. *Adv. Mater.* **2019**, *31*, 1902757.

(8) Ouyang, L.; Chen, K.; Jiang, J.; Yang, X.-S.; Zhu, M. Hydrogen storage in light-metal based systems: A review. *J. Alloys Compd.* **2020**, *829*, No. 154597.

(9) Ley, M. B.; Jepsen, L. H.; Lee, Y.-S.; Cho, Y. W.; Bellosta von Colbe, J. M.; Dornheim, M.; Rokni, M.; Jensen, J. O.; Sloth, M.; Filinchuk, Y.; Jørgensen, J. E.; Besenbacher, F.; Jensen, T. R. Complex hydrides for hydrogen storage−new perspectives. *Mater. Today* **2014**, *17*, 122−128.

(10) Zhang, H.; Xia, G.; Zhang, J.; Sun, D.; Guo, Z.; Yu, X. Graphene-tailored thermodynamics and kinetics to fabricate metal borohydride nanoparticles with high purity and enhanced reversibility. *Adv. Energy Mater.* **2018**, *8*, 1702975.

(11) Li, C.; Peng, P.; Zhou, D. W.; Wan, L. Research progress in $LiBH_4$ for hydrogen storage: A review. *Int. J. Hydrogen Energy* **2011**, *36*, 14512−14526.

(12) Puszkiel, J.; Gasnier, A.; Amica, G.; Gennari, F. Tuning $LiBH_4$ for hydrogen storage: destabilization, additive, and nanoconfinement approaches. *Molecules* **2020**, *25*, 163.

(13) Wang, S.; Gao, M.; Yao, Z.; Liu, Y.; Wu, M.; Li, Z.; Liu, Y.; Sun, W.; Pan, H. A nanoconfined-$LiBH_4$ system using a unique multifunctional porous scaffold of carbon wrapped ultrafine Fe_3O_4 skeleton for reversible hydrogen storage with high capacity. *Chem. Eng. J.* **2022**, *428*, No. 131056.

(14) Li, Z.; Gao, M.; Wang, S.; Zhang, X.; Gao, P.; Yang, Y.; Sun, W.; Liu, Y.; Pan, H. In-situ introduction of highly active TiO for enhancing hydrogen storage performance of $LiBH_4$. *Chem. Eng. J.* **2022**, *433*, No. 134485.

(15) Saldan, I. A prospect for $LiBH_4$ as on-board hydrogen storage. *Cent. Eur. J. Chem.* **2011**, *9*, 761−775.

(16) Yan, Y.; Li, H.; Maekawa, H.; Miwa, K.; Towata, S.-i.; Orimo, S.-i. Formation of Intermediate Compound $Li_2B_{12}H_{12}$ during the Dehydrogenation Process of the $LiBH_4$−MgH_2 System. *J. Phys. Chem. C* **2011**, *115*, 19419−19423.

(17) Karimi, F.; Riglos, M. V. C.; Santoru, A.; Hoell, A.; Raghuwanshi, V. S.; Milanese, C.; Bergemann, N.; Pistidda, C.; Nolis, P.; Baro, M. D.; Gizer, G.; Le, T.-T.; Pranzas, P. K.; Dornheim, M.; Klassen, T.; Schreyer, A.; Puszkiel, J. *In-situ* formation of TiB_2 nanoparticles for enhanced dehydrogenation/hydrogenation reaction kinetics of $LiBH_4$−MgH_2 as a reversible solid-state hydrogen storage composite system. *J. Phys. Chem. C* **2018**, *122*, 11671−11681.

(18) Ding, Z.; Li, S.; Zhou, Y.; Chen, Z.; Yang, W.; Ma, W.; Shaw, L. $LiBH_4$ for hydrogen storage - New perspectives. *Nano Mater. Sci.* **2020**, *2*, 109−119.

(19) Wang, X.; Xiao, X.; Liang, Z.; Zhang, S.; Qi, J.; Lv, L.; Piao, M.; Zheng, J.; Chen, L. Ultrahigh reversible hydrogen capacity and synergetic mechanism of $2LiBH_4$-MgH_2 system catalyzed by dual-metal fluoride. *Chem. Eng. J.* **2022**, *433*, No. 134482.

(20) Xia, G.; Tan, Y.; Wu, F.; Fang, F.; Sun, D.; Guo, Z.; Huang, Z.; Yu, X. Graphene-wrapped reversible reaction for advanced hydrogen storage. *Nano Energy* **2016**, *26*, 488−495.

(21) Bösenberg, U.; Doppiu, S.; Mosegaard, L.; Barkhordarian, G.; Eigen, N.; Borgschulte, A.; Jensen, T. R.; Cerenius, Y.; Gutfleisch, O.; Klassen, T.; Dornheim, M.; Bormann, R. Hydrogen sorption properties of MgH_2−$LiBH_4$ composites. *Acta Mater.* **2007**, *55*, 3951−3958.

(22) Xiao, X.; Shao, J.; Chen, L.; Kou, H.; Fan, X.; Deng, S.; Zhang, L.; Li, S.; Ge, H.; Wang, Q. Effects of NbF_5 addition on the de/rehydrogenation properties of $2LiBH_4$/MgH_2 hydrogen storage system. *Int. J. Hydrogen Energy* **2012**, *37*, 13147−13154.

(23) Gosalawit-Utke, R.; Milanese, C.; Javadian, P.; Jepsen, J.; Laipple, D.; Karmi, F.; Puszkiel, J.; Jensen, T. R.; Marini, A.; Klassen, T.; Dornheim, M. Nanoconfined $2LiBH_4$−MgH_2−$TiCl_3$ in carbon aerogel scaffold for reversible hydrogen storage. *Int. J. Hydrogen Energy* **2013**, *38*, 3275−3282.

(24) Wang, J.; Han, S.; Zhang, W.; Liang, D.; Li, Y.; Zhao, X.; Wang, R. Effects of MoS_2 addition on the hydrogen storage properties of $2LiBH_4$−MgH_2 systems. *Int. J. Hydrogen Energy* **2013**, *38*, 14631−14637.

(25) Gosalawit-Utke, R.; Milanese, C.; Javadian, P.; Girella, A.; Laipple, D.; Puszkiel, J.; Cattaneo, A. S.; Ferrara, C.; Wittayakhun, J.; Skibsted, J.; Jensen, T. R.; Marini, A.; Klassen, T.; Dornheim, M. $2LiBH_4$−MgH_2−$0.13TiCl_4$ confined in nanoporous structure of carbon aerogel scaffold for reversible hydrogen storage. *J. Alloys Compd.* **2014**, *599*, 78−86.

(26) Wang, J.; Han, S.; Wang, Z.; Ke, D.; Liu, J.; Ma, M. Enhanced hydrogen storage properties of the $2LiBH_4$–MgH_2 composite with $BaTiO_3$ as an additive. *Dalton Trans.* **2016**, *45*, 7042–7048.
(27) Puszkiel, J.; Gennari, F. C.; Arneodo Larochette, P.; Troiani, H. E.; Karimi, F.; Pistidda, C.; Gosalawit–Utke, R.; Jepsen, J.; Jensen, T. R.; Gundlach, C.; Tolkiehn, M.; Bellosta von Colbe, J.; Klassen, T.; Dornheim, M. Hydrogen storage in Mg–$LiBH_4$ composites catalyzed by FeF_3. *J. Power Sources* **2014**, *267*, 799–811.
(28) Shao, J.; Xiao, X.; Chen, L.; Fan, X.; Li, S.; Ge, H.; Wang, Q. Enhanced hydriding–dehydriding performance of $2LiBH_4$–MgH_2 composite by the catalytic effects of transition metal chlorides. *J. Mater. Chem.* **2012**, *22*, 20764–20772.
(29) Huang, X.; Xiao, X.; Shao, J.; Zhai, B.; Fan, X.; Cheng, C.; Li, S.; Ge, H.; Wang, Q.; Chen, L. Building robust architectures of carbon-wrapped transition metal nanoparticles for high catalytic enhancement of the $2LiBH_4$-MgH_2 system for hydrogen storage cycling performance. *Nanoscale* **2016**, *8*, 14898–14908.
(30) Huang, X.; Xiao, X.; Wang, X.; Yao, Z.; Wang, C.; Fan, X.; Chen, L. Highly synergetic catalytic mechanism of Ni@g-C_3N_4 on the superior hydrogen storage performance of Li-Mg-B-H system. *Energy Storage Mater.* **2018**, *13*, 199–206.
(31) Zhao, Y.; Ding, L.; Zhong, T.; Yuan, H.; Jiao, L. Hydrogen storage behavior of $2LiBH_4$/MgH_2 composites improved by the catalysis of CoNiB nanoparticles. *Int. J. Hydrogen Energy* **2014**, *39*, 11055–11060.
(32) Zhang, W.; Zhang, X.; Huang, Z.; Li, H.-W.; Gao, M.; Pan, H.; Liu, Y. Recent development of lithium borohydride-based materials for hydrogen storage. *Adv. Energy Sustain. Res.* **2021**, *2*, 2100073.
(33) Jepsen, J.; Capurso, G.; Puszkiel, J.; Busch, N.; Werner, T.; Milanese, C.; Girella, A.; Bellosta von Colbe, J.; Dornheim, M.; Klassen, T. Effect of the process parameters on the pnergy transfer during the synthesis of the $2LiBH_4$-MgH_2 reactive hydride composite for hydrogen storage. *Metals* **2019**, *9*, 349.
(34) Zhao, S.; Wang, Y.; Dong, J.; He, C.-T.; Yin, H.; An, P.; Zhao, K.; Zhang, X.; Gao, C.; Zhang, L.; Lv, J.; Wang, J.; Zhang, J.; Khattak, A. M.; Khan, N. A.; Wei, Z.; Zhang, J.; Liu, S.; Zhao, H.; Tang, Z. Ultrathin metal–organic framework nanosheets for electrocatalytic oxygen evolution. *Nat. Energy* **2016**, *1*, 16184.
(35) Wang, Y.; Liu, Y.; Wang, H.; Liu, W.; Li, Y.; Zhang, J.; Hou, H.; Yang, J. Ultrathin NiCo-MOF nanosheets for high-performance supercapacitor electrodes. *ACS Appl. Energy Mater.* **2019**, *2*, 2063–2071.
(36) Mesbah, A.; Rabu, P.; Sibille, R.; Lebègue, S.; Mazet, T.; Malaman, B.; François, M. From hydrated $Ni_3(OH)_2(C_8H_4O_4)_2(H_2O)_4$ to anhydrous $Ni_2(OH)_2(C_8H_4O_4)$: Impact of structural transformations on magnetic properties. *Inorg. Chem.* **2014**, *53*, 872–881.
(37) Zhou, S.; Wen, M.; Wang, N.; Wu, Q.; Wu, Q.; Cheng, L. Highly active NiCo alloy hexagonal nanoplates with crystal plane selective dehydrogenation and visible-light photocatalysis. *J. Mater. Chem.* **2012**, *22*, 16858–16864.
(38) Huang, X.; Xiao, X.; Wang, X.; Yao, Z.; He, J.; Fan, X.; Chen, L. In-situ formation of ultrafine $MgNi_3B_2$ and TiB_2 nanoparticles: Heterogeneous nucleating and grain coarsening retardant agents for magnesium borate in Li–Mg–B–H reactive hydride composite. *Int. J. Hydrogen Energy* **2019**, *44*, 27529–27541.
(39) Kukula, P.; Gabova, V.; Koprivova, K.; Trtik, P. Selective hydrogenation of unsaturated nitriles to unsaturated amines over amorphous CoB and NiB alloys doped with chromium. *Catal. Today* **2007**, *121*, 27–38.
(40) Manfrinetti, P.; Pani, M.; Dhar, S. K.; Kulkarni, R. Structure, transport and magnetic properties of $MgNi_3B_2$. *J. Alloys Compd.* **2007**, *428*, 94–98.
(41) Le, T. T.; Pistidda, C.; Puszkiel, J.; Castro Riglos, M. V.; Dreistadt, D. M.; Klassen, T.; Dornheim, M. Enhanced hydrogen storage properties of Li-RHC system with in-house synthesized $AlTi_3$ nanoparticles. *Energies* **2021**, *14*, 7853.

https://doi.org/10.1021/acsaem.2c01142
ACS Appl. Energy Mater. XXXX, XXX, XXX–XXX